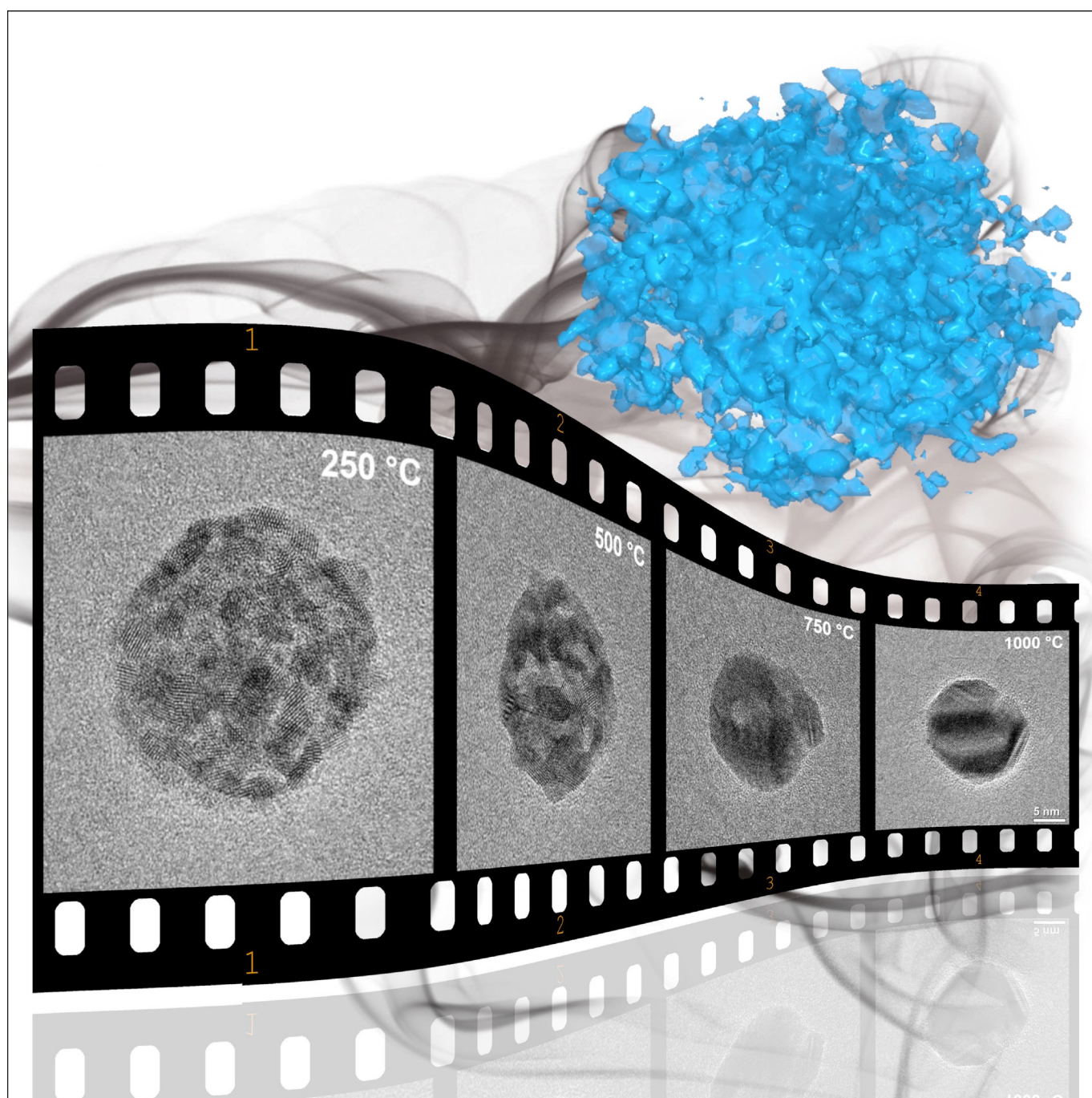


Materials Chemistry

Nanoscale Porous Iridium/Iridium Dioxide Superstructures (15 nm): Synthesis and Thermal Conversion by In Situ Transmission Electron Microscopy

Kevin Pappert^{+, [a]}, Kateryna Loza^{+, [a]}, Meital Shviro,^[b] Ulrich Hagemann,^[c] Marc Heggen,^[d] Rafal E. Dunin-Borkowski,^[d] Roland Schierholz,^[e] Takuya Maeda,^[f] Kenji Kaneko,^[f] and Matthias Eppel^{*[a]}



Abstract: Porous particle superstructures of about 15 nm diameter, consisting of ultrasmall nanoparticles of iridium and iridium dioxide, are prepared through the reduction of sodium hexachloridoiridate(+IV) with sodium citrate/sodium borohydride in water. The water-dispersible porous particles contain about 20 wt% poly(*N*-vinylpyrrolidone) (PVP), which was added for colloidal stabilization. High-resolution transmission electron microscopy confirms the presence of both iridium and iridium dioxide primary particles (1–2 nm) in each porous superstructure. The internal porosity (≈ 58 vol%) is demonstrated by electron tomography. In situ

transmission electron microscopy up to 1000 °C under oxygen, nitrogen, argon/hydrogen (all at 1 bar), and vacuum shows that the porous particles undergo sintering and subsequent compaction upon heating, a process that starts at around 250 °C and is completed at around 800 °C. Finally, well-crystalline iridium dioxide is obtained under all four environments. The catalytic activity of the as-prepared porous superstructures in electrochemical water splitting (oxygen evolution reaction; OER) is reduced considerably upon heating owing to sintering of the pores and loss of internal surface area.

Introduction

The platinum-group metal iridium is one of the rarest non-radioactive metals on earth. Nevertheless, iridium nanoparticles are of high interest in current materials science owing to their promising electrochemical properties, mainly as electrodes for water splitting,^[1] oxygen reduction in fuel cells,^[2] or as catalytic sensors,^[3] for which a high specific surface area is always beneficial.

However, the synthesis of well-faceted nanostructures of iridium is difficult. This can be ascribed to the comparatively low energy barrier of a homogeneous nucleation compared with a heterogeneous nucleation in the case of iridium. Newly formed iridium atoms tend to self-nucleate, which results in small branched particles rather than well-defined faceted structures.^[4] Consequently, only small quasi-spherical or branched structures are obtained through various synthetic routes.^[5] In general, iridium nanoparticles can be synthesized by different reaction pathways. If the synthesis is performed in water, a

strong reducing agent is required because the commonly used precursor complex hexachloridoiridate(+IV), $[\text{Ir}^{\text{IV}}\text{Cl}_6]^{2-}$, has comparatively strong Ir–Cl bonds. Several approaches have been described to reduce this iridium complex to iridium nanoparticles, for example, by superhydride (lithium triethylborohydride)^[5a] or in imidazolium-based ionic liquids.^[5c] Iridium nanoparticles can also be synthesized by the polyol process, in which a polyalcohol serves as both solvent and reducing agent.^[5b]

Porous nanoparticles are of particularly high interest in heterogeneous catalysis owing to their high specific surface area, which is associated with the inner surface.^[6] Han et al. reported a significantly improved oxygen reduction activity of hollow Pd–Pt alloy nanocrystals in comparison with core–shell nanoparticles and with a commercial Pt/C catalyst.^[7] Xia et al. found that gold-based nanocages are more efficient than nanoboxes and solid nanoparticles because of the availability of both internal and external active sites.^[8] However, an ideal catalyst needs not only a high activity, but also sufficient durability under the operating conditions. Thus, it is important to evaluate the stability of particles subjected to thermal stress in a gaseous environment (in situ or operando). Most iridium-based heterogeneous catalytic reactions occur at elevated temperatures, that is, between 60 and 400 °C.^[9]

Here, we present a polyol-based synthesis of porous iridium/iridium dioxide nanoparticles and their in-depth structural analysis by X-ray diffraction, electron tomography, and X-ray photoelectron spectroscopy. Their thermal stability is assessed by in situ high-resolution transmission electron microscopy (HRTEM) under a dynamic gaseous environment at atmospheric pressure.

Results and Discussion

Porous nanoparticles with high specific surface area and high colloidal stability in water were obtained by reduction of $\text{Na}_2[\text{IrCl}_6]$ with sodium citrate/sodium borohydride in the presence of poly(*N*-vinylpyrrolidone) (PVP). Figure 1 shows representative HRTEM and fast Fourier transform (FFT) images. The mostly spherical particles had diameters in the range 10–50 nm and an average diameter of around 15 nm. A higher magnification showed small primary crystallites with sizes be-

[a] Dr. K. Pappert,⁺ Dr. K. Loza,⁺ Prof. Dr. M. Epple
Inorganic Chemistry and Center for Nanointegration Duisburg-Essen (CeNIDE), University of Duisburg-Essen, Universitätsstr. 5–7
45117 Essen (Germany)
E-mail: matthias.epple@uni-due.de

[b] Dr. M. Shviro
Institute of Energy and Climate Research
Electrochemical Process Engineering (IEK-3)
Forschungszentrum Jülich GmbH, 52425 Jülich (Germany)

[c] Dr. U. Hagemann
Interdisciplinary Center for Analytics on the Nanoscale (ICAN) and
Center for Nanointegration Duisburg-Essen (CeNIDE), University of
Duisburg-Essen, Carl-Benz-Strasse 199, 47057 Duisburg (Germany)

[d] Dr. M. Heggen, Prof. Dr. R. E. Dunin-Borkowski
Ernst Ruska-Centre for Microscopy and Spectroscopy with Electrons
Forschungszentrum Jülich GmbH, 52425 Jülich (Germany)

[e] Dr. R. Schierholz
Institute of Energy and Climate Research, Fundamental Electrochemistry
(IEK-9), Forschungszentrum Jülich GmbH, 52425 Jülich (Germany)

[f] Dr. T. Maeda, Prof. Dr. K. Kaneko
Department of Materials Science and Engineering
Kyushu University, 744, Motooka, Nishi, Fukuoka, 819-0395 (Japan)

[⁺] These authors contributed equally to this work.

 Supporting information and the ORCID identification number(s) for the author(s) of this article can be found under:
<https://doi.org/10.1002/chem.201901623>

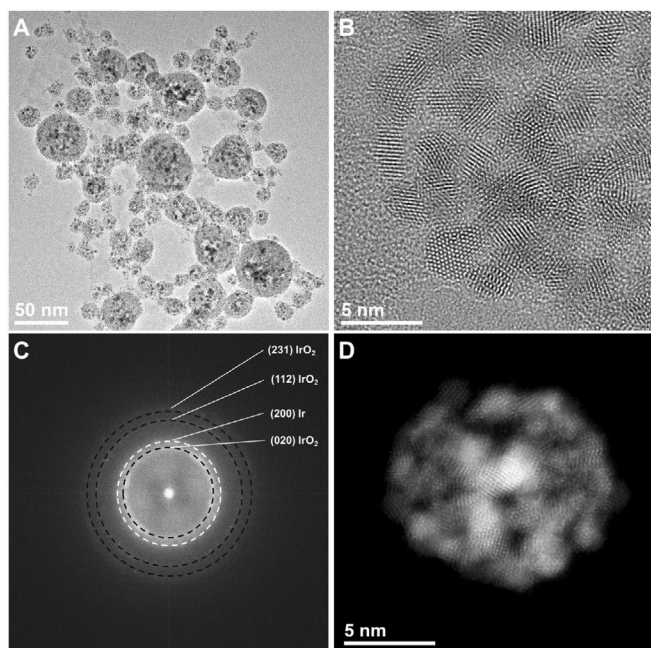


Figure 1. A–C) TEM overview, HRTEM, and corresponding FFT images of porous iridium superstructures (10–50 nm), consisting of small primary crystals (1–3 nm); D) HAADF-STEM image of a single porous superstructure, showing both pores and crystalline domains of primary particles.

tween 1 and 3 nm, forming a porous superstructure. The FFT image of such a porous superstructure showed the (020), (112), and (231) diffraction rings of iridium dioxide and the (200) diffraction ring of metallic iridium. This indicates that an intimate composite structure of metallic iridium and iridium dioxide constitutes the larger porous superstructures. The superstructures were stable under ultrasonication and well dispersible in water. The primary particles appear to be intergrown, but have different crystallographic orientations. Note that the particles were prepared in the presence of PVP, which is still present on their external and internal surfaces (see below). In the following, we will refer to the large spherical particles as “porous iridium superstructures” and to the constituting crystals as “primary crystals”.

To visualize the three-dimensional organization of the primary nanoparticles inside the spherical superstructure, we performed high-angle annular dark-field (HAADF) STEM tomography. Isosurface rendering of a volumetric dataset showed internal voids within the superstructure, probably filled with organic material (PVP), and confirmed its porous nature (Figure 2). Setting the rendering parameters to full opacity and low intensity (A), only the exterior of the surface contour was exposed. Upon decreasing the opacity and increasing the intensity of the surface contour (B–F), the internal contours of the primary particles become distinguishable. Volumetric integration led to a porosity of approximately 58 vol%.

X-ray powder diffraction together with Rietveld refinement gave the overall crystallographic properties of a sample containing more particles than investigated in the electron microscopic study (Figure 3). The refinement showed a two-phase system with peaks of iridium (fcc lattice) as well as iridium di-

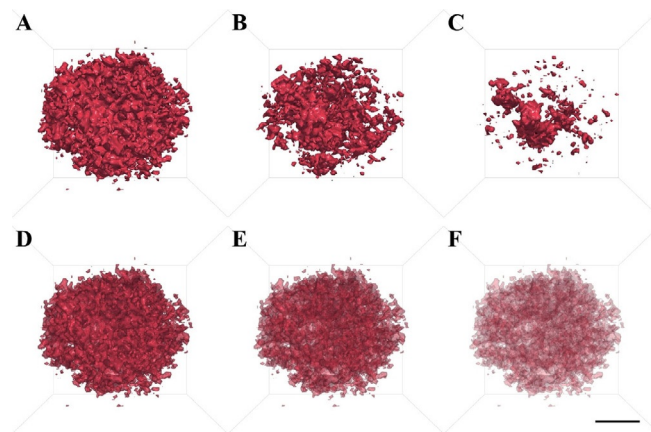


Figure 2. Visualization of a tomographic reconstruction of a porous iridium superstructure (diameter 20 nm). Opacity and intensity of the particle isosurface were varied to elucidate the interior of the nanoparticle: A) Intensity 2, opacity 1.0; B) intensity 2.5, opacity 1.0; C) intensity 3, opacity 1.0; D) intensity 2, opacity 0.5; E) intensity 2, opacity 0.25; F) intensity 2, opacity 0.1. Scale bar: 5 nm.

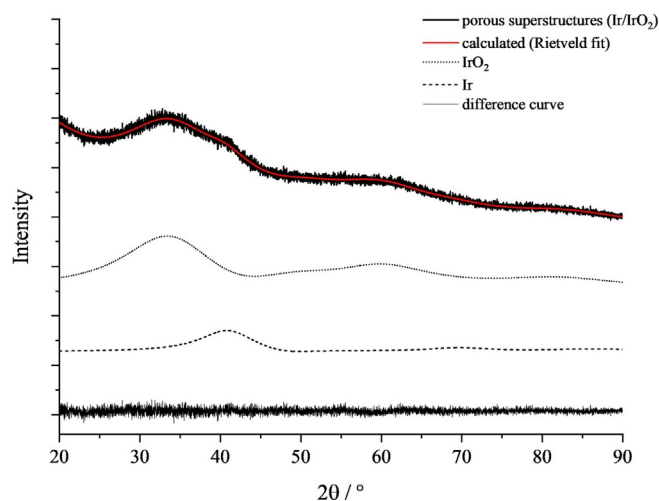


Figure 3. Rietveld refinement of the X-ray diffraction pattern of the porous iridium superstructures. Both iridium and iridium dioxide can be detected, but the peaks are very broad owing to the small size of the primary crystals (≤ 1 nm).

oxide (tetragonal rutile structure), confirming the FFT data from HRTEM. A strong peak broadening was caused by the small size of the primary crystals. Rietveld refinement gave average crystallite sizes of $1.0(\pm 0.1)$ nm for iridium and $0.7(\pm 0.1)$ nm for iridium dioxide, in good agreement with the HRTEM results. The measured lattice constant of metallic iridium ($a = 3.820(\pm 0.007)$ Å) is smaller than that in bulk iridium metal (3.839 Å), an observation that is not uncommon for ultrasmall metal nanoparticles.^[10] The lattice constants for iridium dioxide could not be reliably determined owing to the very broad diffraction peaks. However, phase analysis by Rietveld refinement gave an approximate molar ratio of 28% iridium to 72% iridium dioxide (see Table 2).

X-ray photoelectron spectroscopy (XPS) confirmed the presence of both metallic iridium and iridium dioxide. However, the presence of about 20 wt% PVP (see the thermogravimetric

results below) strongly attenuated the iridium signals. The cumulative peak profile showed two maxima at 61.7 and 64.5 eV (Figure 4). The observed energies were modelled by peaks of the $4f_{5/2}$ and $4f_{7/2}$ binding energies of iridium(0) and iridium oxide(+IV) as well as traces of the 2s binding energy of sodium(+I). The atomic ratio of iridium(+IV) to Ir^0 was approximately 2:1, in good agreement with the XRD data.

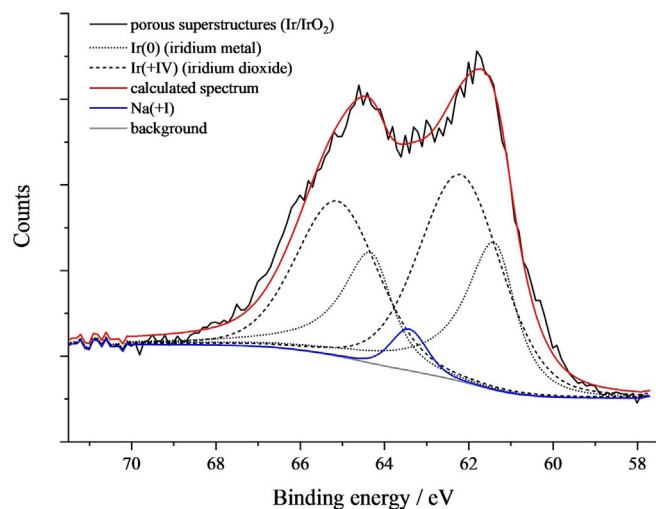


Figure 4. XPS data of the porous iridium superstructures. The spectrum shows 4f peaks of metallic iridium(0) and of iridium dioxide(+IV) as well traces of sodium(+I) (2s peaks).

The traces of sodium probably come from remaining sodium ions from the reducing agents sodium citrate and sodium borohydride that were adsorbed to the particles, probably inside the PVP. The fitted peak positions, and hence, the binding energies of $4f_{7/2}$ and $4f_{5/2}$ are slightly higher than the literature values (Table 1). The shift of the iridium binding energies is 0.3 eV, whereas the shift for iridium oxide is 0.6 eV. Surface modifications or adsorption of organic molecules can lead to a shift in binding energies. The coating of the particles with PVP is a reasonable explanation for this deviation.

Sample	Peak	Binding energy [eV]
porous iridium superstructure	1	61.7
	2	64.5
Ir metal (measured)	$4f_{7/2}$	61.4
	$4f_{5/2}$	64.4
IrO_2 (measured)	$4f_{7/2}$	62.2
	$4f_{5/2}$	65.2
Ir metal ^[11]	$4f_{7/2}$	60.8
	$4f_{5/2}$	63.8
IrO_2 (anhydrous) ^[11]	$4f_{7/2}$	61.9
	$4f_{5/2}$	64.9
IrO_2 (hydrated) ^[11]	$4f_{7/2}$	62.5
	$4f_{5/2}$	65.5

The porous iridium superstructures were colloiddally stable, which is important for their deposition on a substrate such as an electrode. Differential centrifugal sedimentation (DCS) of water-dispersed particles gave a broad size distribution, which was fitted by two Gaussians with maxima at $8(\pm 4)$ nm and $20(\pm 6)$ nm (Figure 5). Note that there is a systematic underesti-

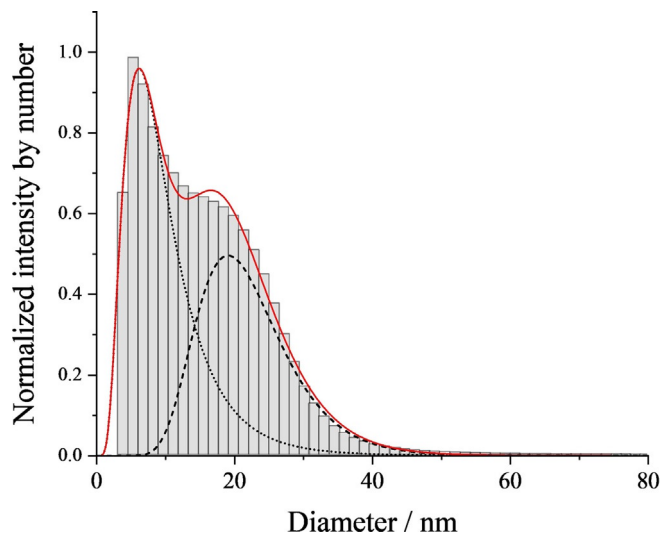


Figure 5. DCS measurement of water-dispersed porous iridium superstructures. The bimodal size distribution was fitted by two independent Gaussians.

mation of the particle diameter by DCS, especially for porous nanoparticles. In DCS, the bulk density of the base material is used to calculate the particle size. However, porous particles have a lower effective density (which is basically unknown), so they sediment more slowly than compact particles of the same size, and the particles appear smaller than they actually are.^[12]

The UV/Vis spectrum of water-dispersed porous superstructures showed a broad absorption band at 584 nm and a steep increase in absorption below 400 nm (Figure 6). This kind of absorption is typical for IrO_2 nanoparticles in dispersion.^[13]

Thermogravimetry under oxygen showed the presence of about 20 wt% volatile/combustible material (i.e., PVP and traces of water) (Figure 7). To elucidate the crystallographic phase composition of the sample during the heating process, batches of the porous iridium superstructures were subjected to annealing, performed in the thermobalance for optimum temperature control. In five different measurements, the superstructures were heated to the final temperatures of 200, 400, 600, 800, and 1000 °C, respectively, and then cooled down rapidly to room temperature (free cooling). Then, the samples were analyzed ex situ by X-ray powder diffraction (Figure 8). The atmosphere was $\text{Ar/O}_2(50:50, \text{vol/vol})$, that is, an oxidizing atmosphere. A marked increase in crystallinity (narrower peaks) between 400 and 600 °C was observed, which can be ascribed to sintering/coalescing of the primary iridium dioxide particles. The diffraction peaks of iridium eventually vanished, either because of oxidation (less likely) or because of the absence of sintering, leading to their disappearance among the increased

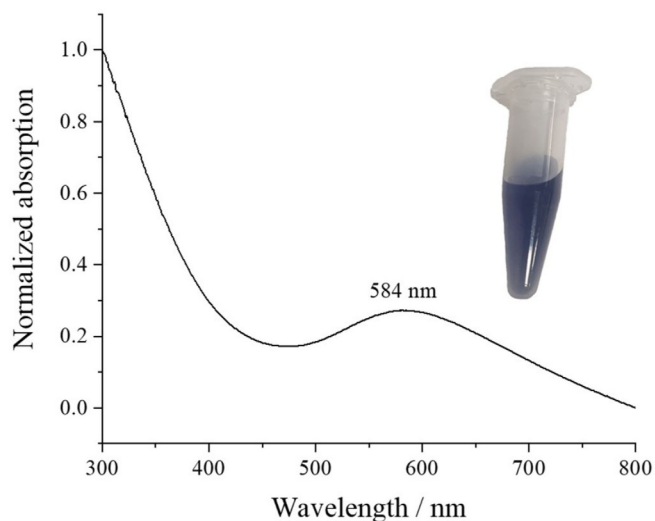


Figure 6. UV/Vis spectrum of water-dispersed porous iridium superstructures, together with an image of the water-dispersed particles that show a characteristic blue–grey color.

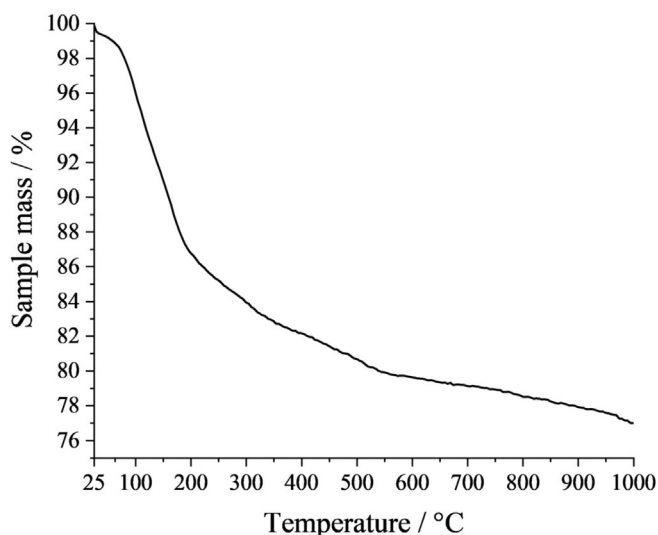


Figure 7. Thermogravimetric analysis of porous iridium superstructures under dynamic oxygen atmosphere. The mass loss is attributed to traces of water and oxidation of PVP (about 20 wt%).

iridium peaks. The derived crystallographic parameters are summarized in Table 2.

Temperature	$a(\text{Ir})$ [Å]	CS(Ir) [nm]	$a(\text{IrO}_2)$ [Å]	$c(\text{IrO}_2)$ [Å]	CS(IrO_2) [nm]	$x(\text{Ir})$ [at %]	$x(\text{IrO}_2)$ [at %]
initial sample	3.820(7)	1.0(1)	–	–	0.7(1)	28	72
200 °C (O_2)	3.8296(6)	2.9(1)	–	–	1.1(1)	35	65
400 °C (O_2)	3.8375(6)	3.4(1)	–	–	1.1(1)	24	76
600 °C (O_2)	3.8421(3)	10.6(2)	4.4906(5)	3.1509(8)	10.6(3)	20	80
800 °C (O_2)	–	–	4.4964(1)	3.1416(1)	22.5(3)	0	100
1000 °C (O_2)	–	–	4.4999(2)	3.1510(2)	63.9(13)	0	100
bulk phases (lit.)	3.8394 ^[14]	–	4.5051 ^[15]	3.1586 ^[15]	–	–	–

[a] All data were obtained by Rietveld refinement. CS: crystallite size.

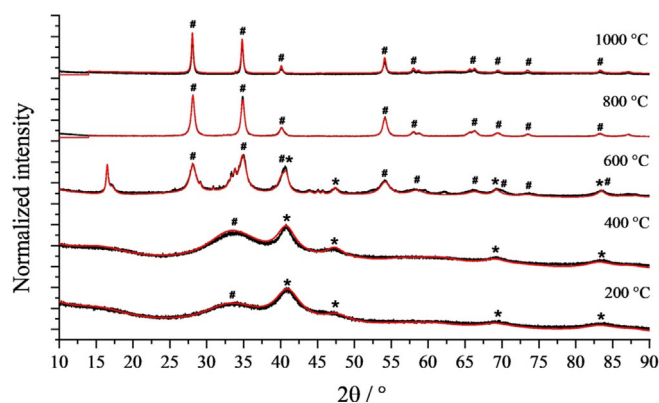


Figure 8. Ex situ X-ray powder diffraction data of porous iridium superstructures after heating under oxygen to the indicated temperature. The particles showed an increase in crystallite size as indicated by the narrowing diffraction peaks. The oxidation of metallic iridium leads to IrO_2 after heating to 800 °C. Black: original data; red: Rietveld refinement. Peaks of iridium are labelled with an asterisk (*), and peaks of IrO_2 are labelled with a hash (#).

The structural details of the thermal transition of the porous iridium superstructures were further elucidated by in situ transmission electron microscopy. As oxidizing or reducing conditions can change the surface properties of a nanoparticle that may be used as catalyst, it is important to verify the actual impact of the real operating conditions on the structure of the metallic nanoparticles. As iridium/iridium dioxide has potential applications in heterogeneous catalysis and the porosity appears especially promising, we have focused on the susceptibility of the porous iridium superstructures to sintering. A nanoreactor setup permitted the observation of the particle evolution in real time under precise temperature and gas control at atomic resolution. We followed the morphological and crystallographic changes in dynamic chemical environments (oxygen, nitrogen, argon/4% hydrogen, all at 1 bar, respectively, and in vacuum) up to 1000 °C.

Bright-field in situ TEM and ex situ HAADF-STEM images demonstrated the structural evolution of the porous iridium superstructures under different environmental conditions (Figures 9–12). In all cases, primary particle growth was observed between 250 and 500 °C. At 750 °C, all porous iridium superstructures had transformed into solid (nonporous) objects with some volume contraction. This process was completed at about 800 to 850 °C (see Supporting Information). At 1000 °C, the particles were compact and consisted of only a few large

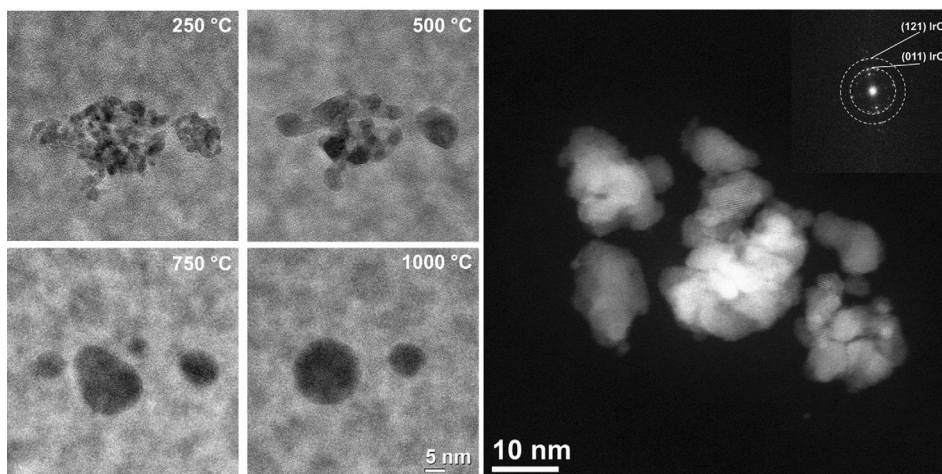


Figure 9. In situ TEM heating under oxygen flow at 1 bar (250, 500, 750, and 1000 °C), and ex situ HAADF-STEM image at 1000 °C and corresponding FFT inset (a time-resolved in situ TEM sequence is available in the Supporting Information). At 1000 °C, the sample consists of sintered iridium dioxide.

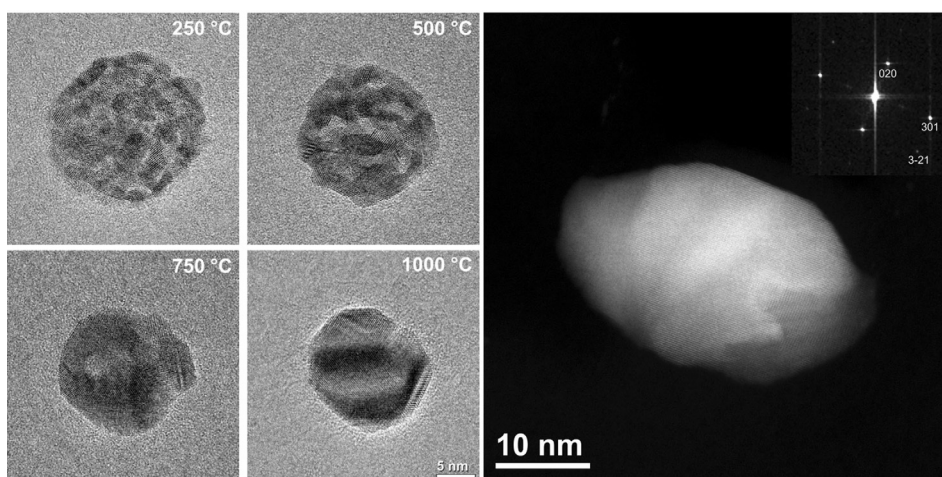


Figure 10. In situ TEM heating in vacuum (250, 500, 750, and 1000 °C), and ex situ HAADF-STEM image after 1000 °C and corresponding FFT inset (a time-resolved in situ TEM sequence is available in the Supporting Information). At 1000 °C, the sample consists of sintered iridium dioxide.

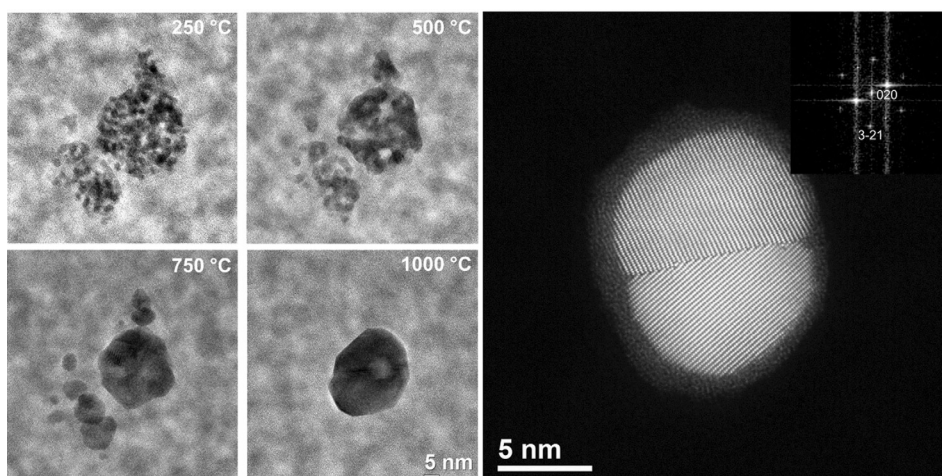


Figure 11. In situ TEM heating under nitrogen flow at 1 bar (250, 500, 750, and 1000 °C), and ex situ HAADF-STEM image after 1000 °C and corresponding FFT inset (a time-resolved in situ TEM sequence is available in the Supporting Information). At 1000 °C, the sample consists of sintered iridium dioxide.

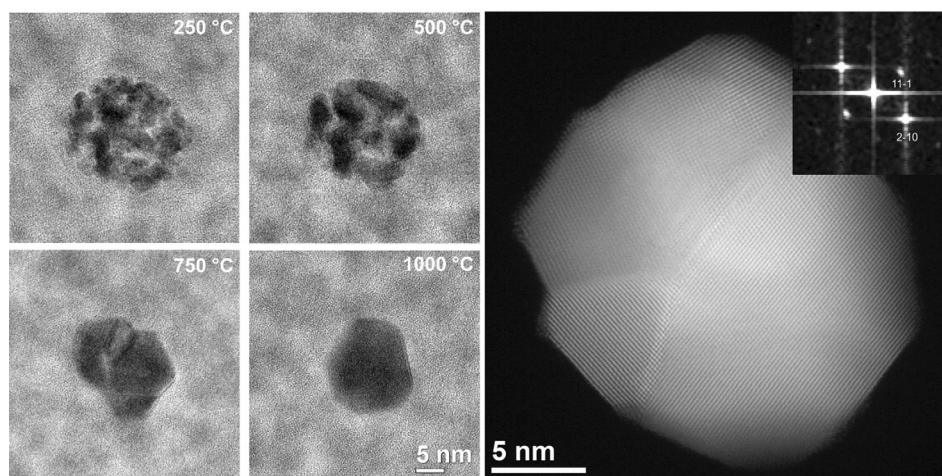


Figure 12. In situ TEM heating under argon/4% hydrogen flow at 1 bar (250, 500, 750, and 1000 °C), and ex situ HAADF-STEM image after 1000 °C and corresponding FFT inset (a time-resolved in situ TEM sequence is available in the Supporting Information). At 1000 °C, the sample consists of sintered iridium dioxide.

domains. The initial porous superstructure consisting of small primary crystals had vanished. This structural evolution is thermodynamically favorable owing to the decrease in free surface energy. Neither disintegration nor generation of smaller particles was observed. It is reasonable to assume that at 1000 °C, the organic component PVP has completely burned under oxygen or undergone pyrolysis under vacuum, inert gas, or reducing conditions.

The particles had a round and compact shape after heating to 1000 °C. FFT analysis confirmed the presence of crystalline IrO₂ in all cases, so the initially present iridium dioxide did not decompose and was not reduced under these conditions, but simply recrystallized. Note that the potential formation of iridium nitride can be excluded in a nitrogen atmosphere under these conditions.^[16] It should also be noted that IrO₂ is oxidized in air to volatile IrO₃ only above 1200 °C, that is, well above the highest temperature in our experimental setup.^[17]

So far, only a few investigations on the thermal behavior of porous nanostructures have been performed using in situ HRTEM. Wang et al. reported a gas-induced change in the surface facets of palladium nanoparticles,^[18] including a surface modification by the “inert gas” nitrogen.^[18b] Edge truncation during reduction and oxidation of palladium nanocubes was detected by in situ TEM.^[18a] With a similar setup, Gao et al. showed a significant change in the surface contact area between metal and support.^[19] Xia et al. reported the thermal stability of faceted Pt-based nanocages under vacuum.^[20] Recently published results of Altantzis et al. showed a quantitative refaceting of Pt nanoparticles in oxygen–hydrogen cycles.^[21] In a reducing environment a more faceted surface was observed. The presence of H₂ and O₂ molecules can result in the promotion or destabilization of certain facets because the surface energy is affected by gas molecule adsorption.^[21,22]

Besides metallic iridium, biphasic systems of iridium and iridium dioxide have high potential in heterogeneous catalysis. Investigations of iridium/iridium dioxide composites by Xu et al. showed a higher electrocatalytic activity compared with

the single-phase materials Ir and IrO₂.^[13a] In general, the mixed oxidation state of iridium shows higher activities in the oxygen evolution reaction (OER) than iridium metal and rutile-type IrO₂ alone.^[23] These biphasic materials have several applications such as stimulating electrodes,^[24] electrodes in water splitting,^[1a,2a] or catalytic sensor systems.^[3a] Iridium oxide fulfills the conditions for operation in a corrosive environment. Therefore, it is an important OER catalyst because of its high activity and stability.^[25]

We tested the porous iridium superstructures in two different states as catalysts for the OER: as-prepared and argon-treated (1000 °C), that is, sintered. TEM images of the samples used in the catalysis showed randomly oriented porous nanoparticles (as-prepared) and dense particles with well-developed facets (1000 °C) (Figure 13). Through STEM-EDX experiments we confirmed that the two samples heated to 1000 °C consisted mainly of iridium dioxide (Figure 14). It was not possible to record meaningful EDX spectra for the as-prepared sample owing to the presence of PVP (high amounts of carbon, oxygen, and nitrogen). This led to an overall oxygen signal that could not be assigned to oxygen from iridium dioxide.

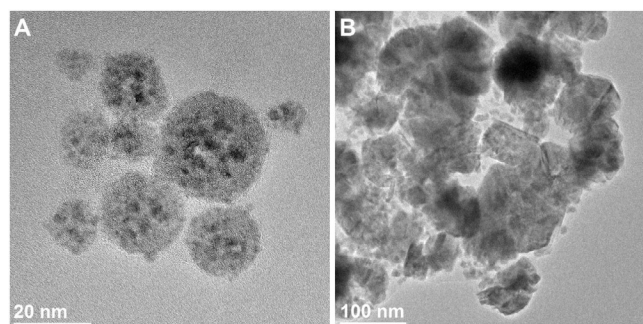


Figure 13. HRTEM images of porous iridium superstructures before OER tests. The samples were A) as-prepared, and B) after heating to 1000 °C in argon. Sample A consists of a mixture of iridium and iridium dioxide, and sample B consists mainly of iridium dioxide.

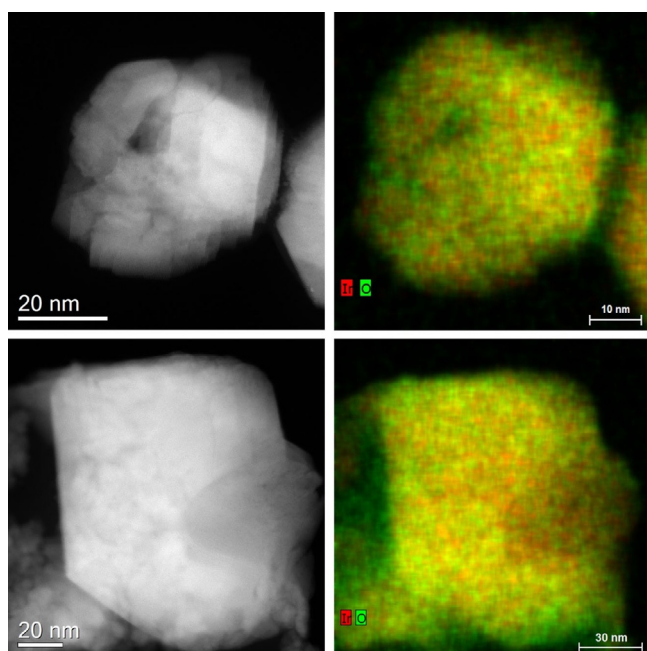


Figure 14. High-angle annular dark field STEM image (left) and EDX map (right) of porous iridium superstructures before OER tests. The as-prepared samples were heated up to 1000 °C in argon (top), and (for comparison) in oxygen (bottom). The samples consist mainly of iridium dioxide, as shown by the high content of oxygen.

Voltammetry showed an increase in the current density for the as-prepared porous superstructures (Figure 15). The previously annealed catalyst (1000 °C) showed a much lower performance, probably because of the increase in crystallite size and particle sintering/compaction. The higher activity of the porous iridium superstructures can thus be explained by the specific surface area (mainly internal surface areas) available for the OER reaction. This is especially remarkable because the as-prepared porous structures still contain PVP, which probably fills the nanopores.

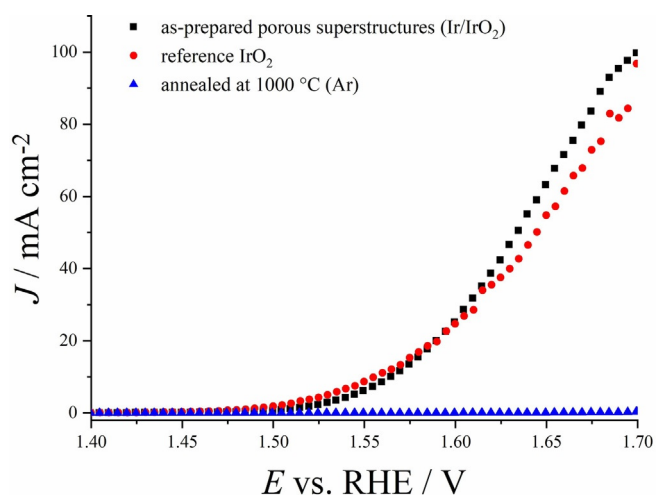


Figure 15. Electrocatalytic OER activities of porous Ir/IrO₂ porous superstructures as-prepared and after heat treatment at 1000 °C in argon. As a control, commercially available iridium dioxide was used.

Conclusions

The thermal stability of porous iridium superstructures, consisting of small nanoparticles of metallic iridium and iridium dioxide, was systematically assessed in different gases (vacuum, oxygen, nitrogen, argon/4% hydrogen) at ambient pressure (1 atm). The porous architecture was stable up to 250 °C for all tested gas mixtures. At higher temperatures, the particles underwent compaction and further faceting, which was completed at about 750 °C. Under oxygen, vacuum, nitrogen, and argon/hydrogen, nanocrystalline iridium dioxide was formed at 1000 °C. The as-prepared porous superstructures were catalytically active in the oxygen evolution reaction, but this property was lost after calcination in argon (1000 °C). We conclude that the high inner porosity of the as-prepared superstructure, associated with a high specific surface area, led to the pronounced catalytic activity.

Experimental Section

Chemicals

For the nanoparticle syntheses, we used poly(*N*-vinyl pyrrolidone) (PVP K 30, Povidon 30; Fluka, $M = 40\,000\text{ g mol}^{-1}$), sodium borohydride (Sigma–Aldrich, $\geq 96\%$, p.a.), and trisodium citrate (Acros, anhydrous 98%). Sodium hexachloroiridate(+IV), Na₂[Ir^{+IV}Cl₆], was obtained from Sigma–Aldrich (p.a.). Ultrapure water (Purelab ultra instrument from ELGA) was used in all experiments. Before use, all glassware was cleaned with boiling aqua regia.

Synthesis of nanoparticles

In a typical synthesis, sodium hexachloroiridate(+IV), Na₂[IrCl₆] (0.02 mmol) was dissolved in water (6.35 mL; metal content 0.719 g L⁻¹, in total 4.57 mg Ir), and was neutralized with 1 M sodium hydroxide solution (20 μL). The solution was then diluted to 250 mL with water and heated to 100 °C under reflux. Then, trisodium citrate (35 mg) was added as a solid. Subsequently, a solution of sodium borohydride (150 mg) dissolved in cold water (10 mL; 4 °C) was added rapidly. After 1 min, a solution of poly(*N*-vinylpyrrolidone) (PVP, 120 mg, $M_w = 40,000\text{ g mol}^{-1}$) in water (10 mL) was added. The mixture was stirred for 35 min under reflux and turned slightly brown. After this period, more sodium borohydride (150 mg) dissolved in cold water (10 mL; 4 °C) was added rapidly. Heating under reflux was continued for another 55 min. Thereafter, the mixture was quenched rapidly to room temperature with an ice bath. The dispersion was stirred for another 48 h at room temperature. The volume of the resulting blue–black dispersion was reduced by vacuum application to 50 mL. The particles were isolated by fourfold ultracentrifugation at 29 400 g (20 000 rpm; 30 min centrifugation time; Sorvall WX Ultra Series instrument), followed by redispersion in water under ultrasonication.

Characterization

Analytical disc centrifugation (differential centrifugal sedimentation; DCS) was performed with a CPS Instruments DC 24 000 disc centrifuge (24 000 rpm). Two sucrose solutions (8 and 24 wt%) formed a density gradient, which was capped with dodecane (0.5 mL) as a stabilizing agent. The calibration standard was a poly(vinyl chloride) (PVC) latex in water with a particle size of 483 nm, provided by CPS Instruments. The calibration was per-

formed prior to each run. A sample volume of 100 μL was used. UV/Vis spectroscopy was performed with a Varian Cary 300 instrument from 200 to 800 nm with background correction. Suprasil[®] cuvettes with a sample volume of 750 μL were used. Freeze-drying (lyophilization) was achieved with a Christ Alpha 2–4 LSC instrument. Thermogravimetric analyses and annealing experiments were performed with a Netzsch TG 449 F3 Jupiter instrument. All measurements were performed in a dynamic gas atmosphere (25 mL min⁻¹) or in vacuum with a heating rate of 5 K min⁻¹ in open alumina crucibles. X-ray photoelectron spectrometry (XPS) was performed with a Physical Electronics PHI 5000 Versaprobe II using aluminum radiation at an energy of 1486.8 eV. A freeze-dried sample was prepared and put onto the sample holder. X-ray powder diffraction (XRPD) was performed on a Bruker D8 Advance diffractometer with CuK _{α} radiation (1.54184 Å) in Bragg–Brentano geometry. A freeze-dried sample was applied to a single-crystal silicon sample holder. Rietveld refinement was performed with the program Topas 5.0 (Bruker). Lorentzian peak profiles were used. Sample displacement error, zero-point error, and instrumental aberrations were all corrected by the addition of LaB₆ (NIST; National Institute of Standards and Technology; SRM 660b; $a(\text{LaB}_6) = 4.15689 \text{ \AA}$) as internal standard.^[26]

The electrochemical characterization in the OER was performed in a rotating disc electrode (RDE) half-cell containing 0.5 M sulfuric acid and equipped with a polished polycrystalline gold working electrode, a platinum counter electrode, and a reversible hydrogen electrode (RHE) connected to the electrochemical cell. The working electrode rotation was controlled with a modulated speed rotator (Pine Instruments), and the electrochemical measurements were recorded with a VMP3 potentiostat (Bio-Logic Science Instruments). The iridium dioxide reference was obtained from Alfa Aesar (IrO₂ powder, 99%) with a primary particle size (from TEM) of 6.5 (\pm 5.3) nm.

HAADF-STEM tomography was performed with a JEOL JEM-ARM200F Cs-corrected S/TEM. For an unobstructed field of view for tomographic data collection a high-tilt angle holder was used. The tilt range was from +66° to -80° with increments of 2°. The sample hydrocarbon contamination was mitigated by a beam shower.^[27] Data alignment by cross-correlation, reconstruction with the weighted backprojection algorithm, and visualization were performed with the *tomviz* software package.^[28]

Scanning transmission electron microscopy (STEM) was performed with an FEI Titan microscope equipped with a Cs-probe corrector (CEOS Company) and a high-angle annular dark field (HAADF) detector. Z-contrast conditions were achieved at a probe semi-angle of 25 mrad and an inner collection angle of the detector of 70 mrad.^[29] The FFT analysis was performed with *CrystBox* (Crystallographic Toolbox).^[30] The elemental mapping by energy-dispersive X-ray spectroscopy (EDX) was conducted on a probe-corrected FEI Titan 80–200 “ChemSTEM” electron microscope equipped with four symmetrical SDD detectors.^[29]

For in situ electron microscopy, a closed gas cell TEM holder (Climate, DENSolutions Company) was used. This nanoreactor consisted of two chips with silicon nitride electron-transparent windows. The bottom chip was equipped with a Pt heater, gas inlet and outlet. For in situ heating experiments in vacuum, a TEM heating holder (Wildfire, DENSolutions Company) and the nano-chip with carbon support were used. All in situ TEM investigations were performed with an aberration-corrected FEI Titan transmission electron microscope equipped with a Cs-probe corrector (CEOS Company), operated at 300 kV.^[31] For the in situ TEM studies, about 12–15 superstructure particles were in the area of interest, but for

clarity, only one is shown. The displayed particles are representative of the whole set of particles in the area of interest.

Acknowledgements

M.E. and M.H. acknowledge financial support of this work by the Deutsche Forschungsgemeinschaft (DFG) in the projects EP 22/44-1 and HE 7192/2-1, 7192/1-1, and 7192/1-2. We thank Martin Gocyla for extensive assistance with the TEM experiments. We thank the Interdisciplinary Center for Analytics at the Nanoscale (ICAN; Duisburg) for the XPS measurements. K.L. is grateful to the Japanese Society for the Promotion of Science for a scholarship. K.K. thanks the Japan Science and Technology Agency (JST) for support (JST-CREST Grant Number JPMJCR18R2).

Conflict of interest

The authors declare no conflict of interest.

Keywords: catalysis · electrochemistry · electron tomography · iridium · transmission electron microscopy

- [1] a) S. D. Tilley, M. Cornuz, K. Sivula, M. Grätzel, *Angew. Chem. Int. Ed.* **2010**, *49*, 6405–6408; *Angew. Chem.* **2010**, *122*, 6549–6552; b) E. Slavcheva, I. Radev, S. Bliznakov, G. Topalov, P. Andreev, E. Budevski, *Electrochim. Acta* **2007**, *52*, 3889–3894.
- [2] a) C. H. Chang, T. S. Yuen, Y. Nagao, H. Yugami, *J. Power Sources* **2010**, *195*, 5938–5941; b) E. Antolini, *ACS Catal.* **2014**, *4*, 1426–1440.
- [3] a) C. Terashima, T. N. Rao, B. V. Sarada, N. Spataru, A. Fujishima, *J. Electroanal. Chem.* **2003**, *544*, 65–74; b) W. D. Huang, H. Cao, S. Deb, M. Chiao, J. C. Chiao, *Sens. Actuators A* **2011**, *169*, 1–11.
- [4] a) X. Xia, L. Figueroa-Cosme, J. Tao, H. C. Peng, G. Niu, Y. Zhu, Y. Xia, *J. Am. Chem. Soc.* **2014**, *136*, 10878–10881; b) Y. Xia, X. Xia, H. C. Peng, *J. Am. Chem. Soc.* **2015**, *137*, 7947–7966.
- [5] a) C. K. Yee, R. Jordan, A. Ulman, H. White, A. King, M. Rafailovich, J. Sokolov, *Langmuir* **1999**, *15*, 3486–3491; b) F. Bonet, K. Tekcia-Elhissen, K. V. Sarathy, *Bull. Mater. Sci.* **2000**, *23*, 165–168; c) G. S. Fonseca, G. Machado, S. R. Teixeira, G. H. Fecher, J. Morais, M. C. Alves, J. Dupont, *J. Colloid Interface Sci.* **2006**, *301*, 193–204.
- [6] a) Y. Lu, L. Yu, M. H. Wu, Y. Wang, X. W. Lou, *Adv. Mater.* **2018**, *30*, 1702875; b) G. Prieto, H. Tuysuz, N. Duyckaerts, J. Knossalla, G. H. Wang, F. Schuth, *Chem. Rev.* **2016**, *116*, 14056–14119; c) M. Tai, E. Havakshian, F. Hasheminasab, *RSC Adv.* **2017**, *7*, 47049–47055.
- [7] J. W. Hong, S. W. Kang, B. S. Choi, D. Kim, S. B. Lee, S. W. Han, *ACS Nano* **2012**, *6*, 2410–2419.
- [8] J. Zeng, Q. Zhang, J. Y. Chen, Y. N. Xia, *Nano Lett.* **2010**, *10*, 30–35.
- [9] a) H. G. Alt, I. K. Bohmer, *Angew. Chem. Int. Ed.* **2008**, *47*, 2619–2621; *Angew. Chem.* **2008**, *120*, 2659–2661; b) J. Dupont, G. S. Fonseca, A. P. Umpierre, P. F. P. Fichtner, S. R. Teixeira, *J. Am. Chem. Soc.* **2002**, *124*, 4228–4229; c) C. Liu, M. Carmo, G. Bender, A. Everwand, T. Lickert, J. L. Young, T. Smolinka, D. Stolten, W. Lehnert, *Electrochem. Commun.* **2018**, *97*, 96–99; d) L. Santacruz, S. Donnici, A. Granados, A. Shafir, A. Vallribera, *Tetrahedron* **2018**, *74*, 6890–6895; e) H. R. Yu, N. Danilovic, Y. Wang, W. Willis, A. Poozhikunnath, L. Bonville, C. Capuano, K. Ayers, R. Maric, *Appl. Catal. B* **2018**, *239*, 133–146.
- [10] a) W. H. Qi, M. P. Wang, *J. Nanopart. Res.* **2005**, *7*, 51–57; b) C. Solliard, M. Flueli, *Surf. Sci.* **1985**, *156*, 487–494; c) Q. Jiang, L. H. Liang, D. S. Zhao, *J. Phys. Chem. B* **2001**, *105*, 6275–6277; d) B. K. Pandey, *J. Chem. Pharm. Res.* **2017**, *9*, 204–209.
- [11] S. J. Freakley, J. Ruiz-Esquius, D. J. Morgan, *Surf. Interface Anal.* **2017**, *49*, 794–799.
- [12] D. Mahl, J. Diendorf, W. Meyer-Zaika, M. Epple, *Colloids Surf. A* **2011**, *377*, 386–392.

- [13] a) D. Xu, P. Diao, T. Jin, Q. Wu, X. Liu, X. Guo, H. Gong, F. Li, M. Xiang, Y. Ronghai, *ACS Appl. Mater. Interfaces* **2015**, *7*, 16738–16749; b) Y. Zhao, E. A. Hernandez-Pagan, N. M. Vargas-Barbosa, J. L. Dysart, T. E. Mallouk, *J. Phys. Chem. Lett.* **2011**, *2*, 402–406.
- [14] R. W. G. Wyckoff, *Cryst. Struct.* **1963**, *1*, 7.
- [15] A. A. Bolzan, C. Fong, B. J. Kennedy, C. J. Howard, *Acta Crystallogr. Sect. B* **1997**, *53*, 373.
- [16] J. C. Crowhurst, A. F. Goncharov, B. Sadigh, C. L. Evans, P. G. Morrall, J. L. Ferreira, A. J. Nelson, *Science* **2006**, *311*, 1275.
- [17] H. Schäfer, H. J. Heitland, *Z. Anorg. Allg. Chem.* **1960**, *304*, 249–265.
- [18] a) X. Zhang, J. Meng, B. Zhu, J. Yu, S. Zou, Z. Zhang, Y. Gao, Y. Wang, *Chem. Commun.* **2017**, *53*, 13213–13216; b) X. Zhang, J. Meng, B. E. Zhu, W. T. Yuan, H. S. Yang, Z. Zhang, Y. Gao, Y. Wang, *Chem. Commun.* **2018**, *54*, 8587–8590.
- [19] M. Y. Duan, J. Yu, J. Meng, B. E. Zhu, Y. Wang, Y. Gao, *Angew. Chem. Int. Ed.* **2018**, *57*, 6464–6469; *Angew. Chem.* **2018**, *130*, 6574–6579.
- [20] M. Vara, X. Wang, J. Howe, M. F. Chi, Y. N. Xia, *ChemNanoMat* **2018**, *4*, 112–117.
- [21] T. Altantzis, I. Lobato, A. De Backer, A. Béché, Y. Zhang, S. Basak, M. Porcu, Q. Xu, A. Sánchez-Iglesias, L. M. Liz-Marzán, G. Van Tendeloo, S. Van Aert, S. Bals, *Nano Lett.* **2019**, *19*, 477–481.
- [22] M. Cabié, S. Giorgio, C. R. Henry, M. R. Axet, K. Philippot, B. Chaudret, *J. Phys. Chem. C* **2010**, *114*, 2160–2163.
- [23] a) V. Pfeifer, T. E. Jones, J. J. V. Velez, R. Arrigo, S. Piccinin, M. Havecker, A. Knop-Gericke, R. Schlogl, *Chem. Sci.* **2017**, *8*, 2143–2149; b) A. Minguzzi, C. Locatelli, O. Lugaresi, E. Achilli, G. Cappelletti, M. Scavini, M. Coduri, P. Masala, B. Sacchi, A. Vertova, P. Ghigna, S. Rondinini, *ACS Catal.* **2015**, *5*, 5104–5115.
- [24] J. D. Weiland, D. J. Anderson, M. S. Humayun, *IEEE Trans. Biomed. Eng.* **2002**, *49*, 1574–1579.
- [25] a) S. D. Song, H. M. Zhang, X. P. Ma, Z. G. Shao, R. T. Baker, B. L. Yi, *Int. J. Hydrogen Energy* **2008**, *33*, 4955–4961; b) S. Geiger, O. Kasian, B. R. Shrestha, A. M. Mingers, K. J. J. Mayrhofer, S. Cherevko, *J. Electrochem. Soc.* **2016**, *163*, F3132–F3138; c) V. Pfeifer, T. E. Jones, J. J. V. Velez, C. Massue, M. T. Greiner, R. Arrigo, D. Teschner, F. Girgsdies, M. Scherzer, J. Allan, M. Hashagen, G. Weinberg, S. Piccinin, M. Havecker, A. Knop-Gericke, R. Schlogl, *Phys. Chem. Chem. Phys.* **2016**, *18*, 2292–2296.
- [26] International Centre for Diffraction Data (ICDD), *Powder Diffraction File (PDF) 00-034-0427 (LaB₆)*.
- [27] D. R. G. Mitchell, *Micron* **2015**, *73*, 36–46.
- [28] B. Levin, Y. Jiang, E. Padgett, S. Waldon, C. Quammen, C. Harris, R. Hovden, *Microscopy Today* **2018**, *26*, 12–17.
- [29] A. Kovács, R. Schierholz, K. Tillmann, *J. Large Scale Res. Fac.* **2016**, *2*, A43.
- [30] M. Klinger, *J. Appl. Crystallogr.* **2017**, *50*, 1226–1234.
- [31] A. Thust, J. Barthel, K. Tillmann, *J. Large Scale Res. Fac.* **2016**, *2*, A41.

Manuscript received: April 8, 2019

Accepted manuscript online: May 28, 2019

Version of record online: August 1, 2019